

1  
2 **The role of the Indian Ocean sector for prediction of the coupled Indo-Pacific system:**  
3 **Impact of atmospheric coupling**

4 **E.C. Hackert<sup>1</sup>, A.J. Busalacchi<sup>2,3</sup>, J. Carton<sup>3</sup>, R. Murtugudde<sup>1,3</sup>, P. Arkin<sup>1</sup>, and M. N.**  
5 **Evans<sup>1,4</sup>**

6 <sup>1</sup>Earth System Science Interdisciplinary Center, University of Maryland, College Park,  
7 Maryland, USA.

8 <sup>2</sup>University Corporation for Atmospheric Research, Boulder, Colorado, USA.

9 <sup>3</sup>Department of Atmospheric and Oceanic Sciences, University of Maryland, College Park,  
10 Maryland, USA.

11 <sup>4</sup>Department of Geology, University of Maryland, College Park, Maryland, USA.  
12

13 Corresponding author: Eric Hackert ([ehackert@essic.umd.edu](mailto:ehackert@essic.umd.edu))

14 **Key Points:**

- Indian Ocean teleconnections generate off-equatorial easterly winds and curl that act to amplify the oceanic Rossby waves in the Pacific
- These Rossby waves eventually positively impact the eastern Pacific via reflected western boundary then equatorial Kelvin waves
- Coupled hindcasts that include interannual forcing in the Indian Ocean significantly improve ENSO prediction skill from 3-9 months

21 **12/13/2016**

22     **Abstract**

23              Indian Ocean (IO) dynamics impact ENSO predictability by influencing wind and  
24        precipitation anomalies in the Pacific. To test if the upstream influence of the IO improves  
25        ENSO validation statistics, a combination of forced ocean, atmosphere, and coupled models are  
26        utilized. In one experiment, the full tropical Indo-Pacific region atmosphere is forced by  
27        observed interannual SST anomalies. In the other, the IO is forced by climatological SST.  
28        Differences between these two forced atmospheric model experiments spotlight a much richer  
29        wind response pattern in the Pacific than previous studies that used idealized forcing and simple  
30        linear atmospheric models. Weak westerlies are found near the equator similar to earlier  
31        literature. However, at initialization strong easterlies between  $30^{\circ}\text{S}$  to  $10^{\circ}\text{S}$  and  $0^{\circ}\text{N}$  to  $25^{\circ}\text{N}$  and  
32        equatorial convergence of the meridional winds across the entire Pacific are unique findings  
33        from this paper. The large-scale equatorial divergence west of the dateline and northeasterly-to-  
34        northwesterly cross-equatorial flow converging on the equator east of the dateline in the Pacific  
35        are generated from interannual IO SST coupling. In addition, off-equatorial downwelling curl  
36        impacts large-scale oceanic waves (i.e. Rossby waves reflect as western boundary Kelvin  
37        waves). After 3 months, these downwelling equatorial Kelvin waves propagate across the  
38        Pacific and strengthen the NINO3 SST. Eventually Bjerknes feedbacks take hold in the eastern  
39        Pacific which allows this warm anomaly to grow. Coupled forecasts for NINO3 SST anomalies  
40        for 1993-2014 demonstrate that including interannual IO forcing significantly improves  
41        predictions for 3-9 month lead times.

42     **1. Introduction**

43         El Niño/Southern Oscillation (ENSO) is the single most important and societally  
44         impactful mode of global climate variability on interannual time scales (e.g. [*Lau and Nath*,  
45         2003], [*Glantz*, 2001], [*Horel and Wallace*, 1981]) but its prediction still has much to improve  
46         upon (e.g. [*National Academies of Sciences and Medicine*, 2016], [*National Research Council*,  
47         2010]). For example, although six month lead forecasts from June 2014 confidently predicted  
48         strong ENSO warm phase conditions based on heat storage anomalies, an event did not develop,  
49         with the most likely explanation the failure to predict the absence of coupling between the ocean  
50         and the atmosphere [*McPhaden*, 2015].

51         There are several possibilities for this prediction failure which include 1) initial triggering  
52         events (i.e. westerly wind bursts) were out of sync with an amplifying mode and with the typical  
53         El Niño development timing (occurring 1 month earlier than for 1997 event) [*Menkes et al.*,  
54         2014], 2) negative feedbacks such as upwelling ocean waves may have damped warm ENSO sea  
55         surface temperature anomalies (e.g. as happened for the 2002 event [*Hackert et al.*, 2007]), 3)  
56         stronger trade wind easterlies associated with the cool phase of the Pacific Decadal Oscillation  
57         (PDO) could have inhibited migration of the precipitation from the warm pool eastward [*Min et*  
58         *al.*, 2015], and 4) Indian Ocean (IO) dynamics may have anchored deep convection over the  
59         Indo-Pacific warm pool rather than allowing it to anomalously develop and couple with  
60         central/eastern Pacific SST anomalies [*Santoso et al.*, 2012].

61         Here we focus on the last possibility by isolating the impact of the IO atmosphere on the  
62         development of ENSO events. In previous work, [*Wu and Kirtman*, 2004], [*Annamalai et al.*,  
63         2005], and [*Annamalai et al.*, 2010] proposed that cold IO sea surface temperature anomalies  
64         (SSTA) could generate an atmospheric Kelvin wave manifesting as equatorial westerly wind  
65         anomalies over the western Pacific, deepening the thermocline in the eastern Pacific via large-

66 scale oceanic Kelvin wave processes (e.g. [Kessler *et al.*, 1995]), and enhancing an ongoing El  
67 Niño.

68 [Wu and Kirtman, 2004] compared coupled and decoupled general circulation model  
69 (CGCM) experiments to test the impact of the IO on ENSO development. They showed that the  
70 ENSO variability is reduced by a factor of two when the IO is decoupled (0.56°C to 0.27°C).  
71 Composite equatorially averaged SST anomalies over longitude and time for the Pacific show  
72 that maximum coupled SST anomalies at 165°W are located 15° east of those observed in the  
73 uncoupled experiment (as in [Yu *et al.*, 2002]) and eastern upwelling associated with Kelvin  
74 wave arrival is delayed by one month. The dominant period of variability is extended by half a  
75 year by decoupling the IO, inconsistent with earlier work of [Yu *et al.*, 2002]. Using a linear  
76 atmospheric model and idealized SSTA forcing, [Wu and Kirtman, 2004] found that the  
77 influence of the IO is via the convective heating and modulation of the Walker circulation. IO  
78 SST can induce anomalous Walker circulation over the eastern equatorial IO (EEIO) and  
79 western-central Pacific through anomalous heating over the IO. For example, cold IO SST  
80 induces development of anomalous westerlies to the east of Indonesia and easterlies to the west,  
81 producing the atmospheric Kelvin wave pattern and a weakening of the Walker circulation [Wu  
82 and Kirtman, 2004]. Therefore, IO SST forcing results indicate a mechanism that can enhance  
83 westerlies over the western Pacific resulting in development of stronger El Niño conditions.

84 Consistent with these results, [Annamalai *et al.*, 2010] find that El Niño is much stronger  
85 when occurring with Indian Ocean Dipole Zonal Mode (IODZM) and cold SST over the EIO and  
86 in the Indonesian Seas (110°E-140°E, 10°S-0°). Winds are westerly over the Pacific from 130°E  
87 east to 120°W and easterly over Indonesia west to the central IO indicating a weaker Walker  
88 circulation. The eastern Pacific thermocline deepens and SST warms east of the dateline.

89 Precipitation is decreased from the central IO to 160°E in the Pacific and increased just east of  
90 160°E and in the western Pacific. Further experiments with the Linear Baroclinic Model (LBM)  
91 of [Watanabe and Jin, 2003] shows that EIO SST forcing generates an atmospheric Rossby  
92 wave signature in the eastern IO but no signal in the Pacific, similar to the idealized forcing of  
93 IODZM in [Annamalai et al., 2005]. However the impact of the Indonesian Seas (120°E-160°E,  
94 5°S-5°N) on the atmospheric linear model response is surprisingly strong and far reaching. Cold  
95 SST forcing in the Indonesian Seas results in strong negative precipitation anomalies  
96 ([Annamalai et al., 2010] Figure 7b) creating an atmospheric Kelvin response that is evident by  
97 easterlies over Indonesia and strong westerlies stretching to the east over the western equatorial  
98 Pacific.

99 In summary, the IO can have strong influence for ENSO via atmospheric pathways.  
100 Regional coupling of basin-scale IO and Indonesian Seas SSTA force enhanced westerlies over  
101 the entire Pacific and increased ENSO forcing. The proposed mechanism is as follows: cold SST  
102 over the EIO 1) reduces the normal east/west temperature gradient across the Pacific providing  
103 favorable conditions for westerly anomalies to develop, 2) suppresses convection over the  
104 Maritime continent and the resulting atmospheric Kelvin wave forces westerlies to the east, 3)  
105 leads to convergence of the westerlies that enhance western Pacific precipitation, and 4) results  
106 in an increased temperature gradient between Indonesia and the dateline further enhancing  
107 westerlies. These westerlies then lead to downwelling oceanic Kelvin waves further enhancing  
108 the growth of El Niño. Although [Annamalai et al., 2010] conclude that regional IO SST and  
109 heating anomalies are not the primary cause, but rather serve to enhance the development of El  
110 Niño, the IO can have strong influences for ENSO via atmospheric teleconnections.  
111 Unfortunately, all previous studies (i.e. [Wu and Kirtman, 2004], [Annamalai et al., 2005], and

112 [Annamalai *et al.*, 2010], etc.) used idealized SSTA patterns and simplified linear atmospheric  
113 models to show impacts of the IO on the wind field without assessing observed ENSO  
114 predictability.

115 Our approach is to use a combination of ocean-only and coupled models to diagnose the  
116 impact of the IO atmospheric teleconnections to ENSO predictability. We will use similar  
117 techniques as in previous studies ([*Yu et al.*, 2002], [*Wu and Kirtman*, 2004], [*Annamalai et al.*,  
118 2005], [*Annamalai et al.*, 2010], and [*Santoso et al.*, 2012]) to diagnose the impact of the  
119 interannual SSTA forcing in the IO. Namely, we difference results from experiments that fully  
120 couple the SSTA throughout the Indo-Pacific region with ones that decouple the IO by forcing  
121 with climatological SST in this region. Unlike all previous studies, however, we develop  
122 realistic coupled hindcast experiments using realistic interannual anomalies as forcing, and  
123 validate the results against observations of forecasted ENSO state. The overriding hypothesis  
124 that we wish to test is that the upstream influence of the Indian Ocean improves ENSO  
125 predictions through mechanisms associated with the atmospheric bridge as coined by [*Alexander*  
126 *et al.*, 2002]. We will use “atmospheric bridge”, “atmospheric teleconnection” or “atmospheric  
127 impact” interchangeably throughout the following text for this impact.

128 The organization of this paper is as follows. Section 2 covers ocean and coupled models  
129 and Section 3 describes the simulations and analysis techniques. Section 4 reports the various  
130 model results, Section 5 contains the discussion, and Section 6 summarizes the paper results and  
131 provides conclusions.

132

133    **2. Models**

134    **2.1 Ocean Model**

135       The ocean general circulation model (OGCM) that is used in this study is the primitive-  
136       equation, sigma-coordinate model with variable depth oceanic mixed layer of *Gent and Cane*  
137       [1989]. It is described and validated in a series of simulation studies of circulation in all three  
138       tropical ocean basins [*Hackert et al.*, 2001; *Murtugudde and Busalacchi*, 1998; *Murtugudde et*  
139       *al.*, 1996; *Murtugudde et al.*, 1998]. Solar radiation (Earth Radiation Budget Experiment -  
140       ERBE) and interannual precipitation from the Global Precipitation Climate Project - GPCP  
141       [*Adler et al.*, 2003] are specified externally. Monthly anomalies of the cloud data [NCEP  
142       Reanalysis *Kalnay et al.*, 1996] are added to the Interannual Satellite Cloud Climatology Project  
143       –ISCCP annual cycle [*Rossow and Schiffer*, 1991] in order to provide a more realistic mean.

144       Our OGCM uses the hybrid vertical mixing scheme of *Chen et al.* [1994] which  
145       combines the advantages of the traditional bulk mixed layer of *Kraus and Turner* [1967] with the  
146       dynamic instability model of *Price et al.* [1986]. This allows simulation of all three major  
147       processes of oceanic vertical turbulent mixing - atmospheric forcing is related to mixed layer  
148       entrainment/detrainment, gradient Richardson number accounts for shear flow, and instantaneous  
149       adjustment simulates high frequency convection in the thermocline. The vertical structure  
150       consists of a variable depth mixed layer and 19 sigma layers with a deep motionless boundary  
151       being specified as  $T_{bottom} = 6^{\circ}\text{C}$  and  $S_{bottom} = 35 \text{ PSU}$ .

152       The ocean model configuration used for all simulations covers the tropical Indo-Pacific  
153       basin ( $34^{\circ}\text{E}$  - $76^{\circ}\text{W}$ ,  $30^{\circ}\text{S}$ - $30^{\circ}\text{N}$ ) with a homogeneous  $1^{\circ}$  longitudinal grid and a variable  
154       latitudinal grid (down to  $1/3^{\circ}$  within  $10^{\circ}$  of the equator). This resolution is dense enough to allow  
155       mesoscale eddies and realistic flow. Surface fluxes are calculated interactively by coupling the  
156       OGCM to a thermodynamic atmospheric mixed layer model [*Murtugudde et al.*, 1996] thus

157 allowing feedbacks between SST, SSS, and surface fluxes. The open boundaries are treated as a  
158 sponge layer within  $10^{\circ}$  of the north and south borders smoothly relaxing to World Ocean Atlas  
159 2009 (WOA09 - [Antonov *et al.*, 2010]). Note that this model surface is allowed to vary freely as  
160 a natural boundary condition ([Huang, 1993]) and only relaxes back to Levitus temperature and  
161 salinity ([Locarnini *et al.*, 2010]) within the north and south boundary sponge layers.

162 The model is spun up from rest using climatological winds with the initial conditions  
163 derived from WOA09 data and is allowed to come to equilibrium after 30 years of forcing by the  
164 ECMWF [1994] analysis climatology. Interannual runs are initialized from this climatological  
165 spin-up starting in 1975 and the wind speeds required for sensible and latent heat fluxes are  
166 computed from interannual ECMWF 10 m wind converted to stress using the bulk formula ( $\rho =$   
167  $1.2 \text{ kg/m}^3$ ,  $C_D = 1.2 \times 10^3$ ).

## 168 **2.2 Atmospheric Model**

169 An intermediate complexity atmospheric general circulation model (AGCM), the  
170 International Centre for Theoretical Physics AGCM (nicknamed SPEEDY, for “Simplified  
171 Parameterizations, primitivE-Equation DYnamics” - [Molteni, 2003]; [Kucharski *et al.*, 2006])  
172 provides an accurate atmospheric model response, yet is highly computationally efficient. We  
173 use SPEEDY Version 41, which has global T30 resolution (roughly  $3.75^{\circ}$ ) with 8 standard sigma  
174 layers (925 – 30 mb) and surface information. The winds in the tropics have been improved by  
175 adding cumulus momentum transport (CMT) to the convective parameterization code using the  
176 technique of [Kim *et al.*, 2008]. This technique transports momentum downward within  
177 subsidence regions surrounding regions of convection. Adding CMT to the atmospheric model  
178 shifts wind and western Pacific precipitation anomalies eastward, which are more in line with  
179 observations. In addition, the meridional extent of the wind anomalies is expanded due to the

incorporation of the CMT. For example, [Kim *et al.*, 2008] show that 850 mb westerlies during ENSO expand from 15°S-0°N without CMT to 15°S-10°N with CMT. Implementation of CMT has also shown to improve intraseasonal precipitation, SST and winds such as those associated with Madden Julian Oscillations [Zhou *et al.*, 2012]. Hence, effects of the IO on the coupled ENSO system should be distinguishable within SPEEDY simulations via analysis of wind and precipitation anomalies on intraseasonal to interannual timescales.

The winds and precipitation from SPEEDY have similar validation statistics as for other atmospheric models and observations. For example, the mean 925 mb winds of SPEEDY over the tropics closely match the European Centre for Medium-Range Weather Forecasts reanalysis (ERA - [Gibson *et al.*, 1997]). For precipitation, all the major features of the observations (CMAP from [Xie and Arkin, 1998]) are reproduced by SPEEDY. However, the SPCZ has less abundant rainfall and relatively more precipitation over the tropical IO [Molteni, 2003] and SPEEDY tends to underestimate the zonal wind anomalies associated with ENSO events (see Figure 9 of [Kroeger and Kucharski, 2011]). For a full description of latest version of SPEEDY see [Kucharski *et al.*, 2013].

### 2.3 Coupled Model

Coupling of an intermediate complexity atmospheric model such as SPEEDY is justified since the atmospheric time scale is much shorter than that of the ocean. The SPEEDY AGCM has been successfully coupled with other ocean models for the Pacific (e.g. [Kucharski *et al.*, 2011]), Indian ([Kucharski *et al.*, 2006]), and Indo-Pacific regions ([Bracco *et al.*, 2005]). Similar to the implementation of [Kroeger and Kucharski, 2011], we use the technique of anomaly coupling to couple the ocean and atmospheric models. Within the tropical Indo-Pacific region, our ocean model SSTA forces the SPEEDY AGCM. For the rest of the globe, the

observed SSTA of HadISST [Rayner *et al.*, 2003] is used and climatological values are used for other atmospheric model boundary conditions such as surface albedo, climatological SST, sea ice, snow depth, vegetation, heat flux parameters, and soil moisture (matching those described in [Kucharski *et al.*, 2013]). The SST anomaly is formulated with respect to the ECMWF/GPCP climate experiment (described in Section 2.1). The atmospheric model is then spun up for 1 month using this SSTA and anomalies of surface zonal and meridional wind stress ( $\tau'_x$ ,  $\tau'_y$ ) and precipitation ( $P'$ ) are formulated with respect to the mean seasonal cycle over 1993-2014 of the similarly forced atmospheric model. These anomalies are subsequently added back to the ECWMF and GPCP climatologies to force the next month of the ocean model simulation. While more efficient than the operational coupled models which use high resolution and more complete atmospheric models, the coupling of SPEEDY nevertheless allows adequate physics to quantify the impact of the atmospheric bridge on ENSO prediction. Using this technique, one year forecasts are completed for each month for 1993-2014.

In order to validate the coupled model, NINO3 SST anomalies are compared against observations. SPEEDY coupled model has significantly better correlation (Figure 1a) and amplitude validation (Figure 1b) than observational persistence after 4 months and 3.5 months, respectively. The correlation of SPEEDY versus observations remains significant at  $p<0.05$  (df=35) for 8 month lead times. As a forecast skill comparator, we include the Climate Forecast System Reanalysis Reforecast ([Saha *et al.*, 2014]) as a reference (Figure 1 - black line). These coupled hindcasts are comprised of the atmospheric assimilation/model with resolution ~38 km (detailed in [Saha *et al.*, 2010]) along with the MOM4 ocean model ([Griffies *et al.*, 2004]) with 0.5° resolution within 30°N-30°S and the Global Ocean Data Assimilation System (GODAS) ocean assimilation ([Behringer, 2007]) of all available oceanic in situ data. The CFSRR model

226 was chosen to substantiate our coupled model results since it is a well-known, state of the art,  
227 operational coupled model (i.e. the reanalysis, reforecast version of CFSv2). For these long  
228 validation runs (i.e. January 1993 to March 2011), correlation between forecasted and observed  
229 NINO3 SSTAs are equivalent (Figure 1a). For validation by root mean square difference  
230 (RMSD), results from our coupled model outperform the CFSRR for all lead times. CFSRR  
231 RMSD errors reach  $1.4^{\circ}\text{C}$  at 10 month lead times, whereas SPEEDY coupled model RMSD  
232 errors are  $1^{\circ}\text{C}$  for the same lead time. Based on these diagnostics, our coupled model validates at  
233 least as well as the NOAA operational model.

234 **3. Simulations and Analysis**

235 **3.1 Uncoupled Simulations**

236 SSTA is calculated over 1993-2014 from the ocean model that is forced using all  
237 available observed winds, cloudiness, and precipitation (described in Section 2.1). SPEEDY  
238 atmosphere-only experiments are then initiated using different ocean model SSTA for the IO  
239 basin to isolate the ocean forcing impacts via the atmosphere on the coupled Indo-Pacific system.  
240 In this work, the Pacific (abbreviated PAC) is defined as 30°N-30°S, 130°E-70°W and the Indian  
241 Ocean (IO) is defined as 30°N-30°S, 30°E-129°E. Outside the tropical Indo-Pacific region, the  
242 interannual SSTA from the Hadley Centre (HadISST, [Rayner *et al.*, 2003]) is used to force the  
243 global SPEEDY model. Within the Indo-Pacific region, experiments were initiated that are  
244 designed to isolate the impact of the IO region surface forcing on the atmosphere.

245 Table 1 shows the complete set of experiments performed for this study. The  
246 experiments either use interannual (i.e. INT) SSTA forcing or climatology seasonal cycle  
247 (CLIM) SST separated by basin, PAC and IO. For example, forcing SPEEDY using interannual  
248 SSTA for the Pacific and IO is abbreviated as INT\_PAC, INT\_IO. Following the similar  
249 methodology of e.g. [Wu and Kirtman, 2004], we subtract the results from these different  
250 experiments in order to isolate the impact of the IO sector ocean forcing. Thus, subtracting  
251 INT\_PAC, CLIM\_IO results from INT\_PAC, INT\_IO will isolate the impact of the IO SSTA via  
252 the atmospheric teleconnections to the Pacific.

253

254 **3.2 Coupled Simulations**

255 A series of coupled experiments designed to isolate the full impact of the interannual IO  
256 SSTA forcing is executed. Operationally the same initial conditions are used as for the  
257 uncoupled simulations, since the goal is to completely eliminate any potential impacts caused by

258 different initialization. However, within the anomaly coupling procedure we replace the regional  
259 SST anomaly with zeros effectively substituting the forecast interannual SST forcing with  
260 climatological seasonal cycle values. A series of two 12 month coupled experiments were  
261 completed for each month from 1993-2014: for each experiment, a total of 264 12 month runs  
262 were completed. The two experiments are 1) INT\_PAC, INT\_IO (interannual SST anomaly  
263 forcing for the Pacific and the IO) and 2) interannual Pacific, climatological IO (INT\_PAC,  
264 CLIM\_IO). As in the uncoupled experiments (section 3.1), the experiments with similar Pacific  
265 forcing are compared, e.g. INT\_PAC, INT\_IO versus INT\_PAC, CLIM\_IO.

266 **3.3 Analysis Techniques**

267 Unlike all previous similar research, the impact of the IO on ENSO predictability is  
268 evaluated using observed quantities. Specifically, the observed NINO3 ( $5^{\circ}\text{S}$ - $5^{\circ}\text{N}$ ,  $90^{\circ}\text{W}$ - $150^{\circ}\text{W}$ )  
269 SSTA from [Reynolds *et al.*, 2002] is used to validate all coupled and forced model results using  
270 correlation and RMSD. For correlation, the effective degrees of freedom (df) is calculated using  
271 the technique of [Quenouille, 1952] (pp. 168-170) with the equation:  
272 
$$\text{df} = \frac{N}{(1 + 2 * r_a(1) * r_b(1) + 2 * r_a(2) * r_b(2) + 2 * r_a(3) * r_b(3))}$$
 where N is original number of  
273 observations and  $r_a$  and  $r_b$  are autocorrelations for time series a and b, respectively for 1, 2, and 3  
274 months lags (indicated by indices). After the effective degrees of freedom are calculated the  
275 Students T test is used to establish significance of correlation values. For all statistics, a  
276 probability of less than  $p=0.05$  that a correlation is zero will be considered statistically  
277 significant and interpretable. In order to test the impact of the IO atmospheric teleconnections  
278 to ENSO, forecast lead time correlations will be compared between different coupled model  
279 results. Since all experiments are validated against observed SST anomalies, and so share a  
280 common variable, these correlations are not independent (known as correlated correlations).

281 Therefore, the Steiger's Z-test [Steiger, 1980] will be utilized to test the significance of the  
282 differences between correlations as applied in [Uehara *et al.*, 2014]. The details follow:

283 
$$Z = \frac{[Z_{aa} - Z_{ba}] * \sqrt{N-3}}{\sqrt{2*[1-r_{aa}]*h}}$$
 where  $Z_{ao}$ ,  $Z_{bo}$  are Fisher Z transformations of  $r_{ao}$  and  $r_{bo}$  (the

284 correlation of experiments a and b, respectively versus observations (o), N is the number of  
285 observations and  $r_{ab}$  is the correlation between the two forecast experiments, a and b,  $h =$   
 $\frac{1-rr^2}{1-rr^2}$ ,  $f = \frac{1-r_{aa}}{2*[1-rr^2]}$ , and  $rr^2 = \frac{r_{aa}+r_{ab}}{2}$ . This technique has the benefit of producing a

286 statistic that is normally distributed, so for  $|Z| > 1.96$ ,  $p \leq 0.05$ . In addition, the lead time  
287 amplitude of the various forecasts will be validated against observed NINO3 SST anomaly using  
288 RMSD. Forecast standard deviation and mean will also be used to compare different forecasts  
289 versus observed values. The forecast mean (standard deviation) is simply the mean (standard  
290 deviation) across all forecasts, on lead times from 0 to 12 months.

292 In order to quantify the impact of Kelvin and Rossby wave propagation on El Niño  
293 events, sea level anomalies are first converted to geostrophic currents using the methodology of  
294 [Picaut and Tournier, 1991]. Next, the technique derived by [Delcroix *et al.*, 1994] is used to  
295 separate the sea level anomalies geostrophic current data into Kelvin and Rossby components.

296

297 **4. Results**

298 **4.1 Forced Ocean and Atmospheric Model Results**

299 The results of the SPEEDY atmospheric model differences described in Section 3.1 are  
300 designed to isolate the impact of the IO and are presented in Figure 2a-f for zonal and meridional  
301 wind stresses, precipitation, curl and divergence of the wind stress, respectively. By differencing  
302 experiments with full coupling in the IO minus those with decoupled IO, the impact of the  
303 variations in the IO summer monsoon is readily apparent for both precipitation and wind stress.  
304 For precipitation (Figure 2c), positive anomalies can be seen stretching from the equator to 10°N  
305 in the eastern Arabian Sea (AS), at 7°N to 12°N in the Bay of Bengal (BOB), and 10°N to 20°N  
306 in the South China Sea (SCS). Abundant rainfall is consistent with convergence of the monsoon  
307 flow starting south of the equator as southeasterlies, recurving to southerlies near the equator and  
308 decelerating as southwesterlies in the AS, BOB, and SCS (Figure 2d and f). These  
309 southwesterlies converge into northeasterlies found north of 10°N in the BOB and SCS. In the  
310 Southern Hemisphere, between 10°S and the equator, negative precipitation anomalies are  
311 generally found west of 95°E. These precipitation patterns are consistent with the general  
312 divergence of the winds in these regions as they feed into the northward monsoon flow. In  
313 addition, positive precipitation is found over the southern Indonesian islands between 95°E and  
314 130°E stretching between 12°S to 5°S. This feature is due to the onshore convergence of the  
315 westerlies found west of 95°E and is consistent with anomalies that are associated with the  
316 transition of the northwest to summer monsoons in boreal spring. In the southwest IO between  
317 25°S-15°S and west of 80°E, a band of positive precipitation is evident just to the east of  
318 Madagascar and is the result of southeasterlies to the south converging with northwesterlies to  
319 the north (Figure 2f). Warm SST leads to atmospheric advection, enhanced inflow, convergence  
320 and abundant atmospheric convection and precipitation. The patterns in the IO are consistent

321 with the anomalies of the monsoon wind and precipitation patterns (those patterns associated  
322 with interannual minus climatological seasonal cycle SST forcing in the IO).

323 In the Pacific, generally positive precipitation anomalies are found off the equator at 5°N,  
324 15°S centered near 160°W (Figure 2c). In addition, positive anomalies are seen in the upwelling  
325 region of the eastern equatorial Pacific east of 130°W and in the South Pacific Convergence  
326 Zone (SPCZ) at 10°S, 160°E. North of 10°N and south of 20°S, negative precipitation anomalies  
327 are simulated. Strong easterly anomalies can be seen between equator and 20°N and south of  
328 15°S across the entire Pacific basin (Figure 2a). North of 20°N, strong westerly anomalies  
329 prevail. Between 10°S and the equator, wind differences are generally very weak but westerly.  
330 The meridional winds (Figure 2b) converge to roughly 5°S with northerlies to the north and  
331 southerlies to south especially east of the dateline. Along 20°N winds are generally divergent for  
332 the meridional wind plot.

333 **4.2 Coupled Model Results**

334 The validation of the two coupled simulations versus observed NINO3 SSTA over all 12  
335 month lead times, 1993-2014, is presented in Figure 3a. Both simulations are significantly  
336 correlated with observations out to 8 and 5.8 months for INT\_PAC, INT\_IO and INT\_PAC,  
337 CLIM\_IO, respectively. After 3 month lead times, the correlation of the full coupling begins to  
338 outperform the INT\_PAC, CLIM\_IO coupled simulation. Correlation differences climb to  
339  $r=0.16$  by 7 month lead times. At this time the Steiger Z Test ([Steiger, 1980]) shows that the  
340 differences are significant (thick dashed line on top x axis in Figure 3a). After that, the  
341 differences drop to about  $r=0.1$  out to 10 month lead times when the Figure 3 differences are no  
342 longer significant. The important result of this plot is that the interannual forcing of the IO  
343 significantly improves coupled forecasts for ENSO. Results for RMSD of simulated versus

344 observed NINO3 SSTA (Figure 3b) are consistent with results for correlation (Figure 3a) and  
345 quantify the validation error amplitude.

346

347       **5. Discussion**  
348       Over most of the forecast period and particularly between 3 to 9 month lead times,  
349       interannual SST forcing in the IO improves correlation and reduces the RMS differences  
350       between observed NINO3 SSTA and those simulated by the fully coupled model. Therefore,  
351       these results suggest that including the impacts of the IO atmospheric teleconnection serves to  
352       improve the coupled predictability as validated with real observations over 1993 to 2014.

353       The next step is to examine why the interannual SST forcing of the IO improves the  
354       coupled forecasts. Figure 4 shows the mean and standard deviation of the NINO3 SSTA of all  
355       the 12 month forecasts from 1993-2014. The mean plot (Figure 4a) shows that the experiment  
356       with interannual IO forcing has higher mean values (relative warming signal in the NINO3  
357       region) after 3 months. On the other hand, the INT\_PAC, INT\_IO and INT\_PAC, CLIM\_IO  
358       standard deviation lines in Figure 4b practically overlay one another. This result is different than  
359       that of [Santoso *et al.*, 2012] and [Wu and Kirtman, 2004] who found that the IO increased the  
360       amplitude of ENSO events. On the contrary, we conclude that the interannual signal in the IO  
361       serves to warm the mean state in the eastern Pacific after 3 months rather than impact the  
362       variability.

363       To further diagnose the source of the warming after 3 months, the mean forecast  
364       difference, INT\_PAC, INT\_IO minus INT\_PAC, CLIM\_IO, is presented for all 12 months of  
365       lead times. Equatorial longitude versus time plots track the evolution over the average forecast  
366       in Figure 5. Early in the average forecast difference, prior to month 3, easterly winds along the  
367       equator between 140°E-160°E and between 180°-140°W (Figure 5c) set off upwelling Kelvin  
368       waves (Figure 6a), cooling SSTA (Figure 5a), and inducing westward flow across the entire  
369       Pacific (Figure 5d). This is consistent with the general upwelling favorable curl in the initial  
370       conditions (Figure 2e) between 15°S-10°N. After this slight upwelling and cooling in the central

371 Pacific associated with equatorial easterlies, the SST in the NINO3 region begins to warm after 3  
372 month lead times (Figure 5a). In the east, westerlies centered at approximately 130°W generate  
373 a downwelling Kelvin wave that arrives at the eastern boundary at month 4 (Figure 6a). At this  
374 time the NINO3 region begins to warm (Figure 5a). In the west, westerlies on the equator west  
375 of 140°E and near the dateline act in the equatorial Pacific setting off a second downwelling  
376 Kelvin wave, which is identified by positive sea level anomaly and eastward flow (Figure 5b, d  
377 and Figure 6a) that starts in month 4 and traverses the Pacific and arrives at the eastern boundary  
378 by month 6. The cumulative effects of the downwelling Kelvin waves after month 5 are to  
379 continue to warm the NINO3 region. For month 6 through 8, warmest SSTA is building in the  
380 central Pacific between 160°E and 140°W. Westerlies to the west and easterlies to the east  
381 converge into this warm region (Figure 5c) near the dateline. A weak upwelling Kelvin wave  
382 (Figure 6a dashed line) is initiated that is associated with these easterlies east of the dateline. At  
383 this time, the prevailing eastward flow is interrupted and westward currents are found in the  
384 eastern Pacific between months 6-8 (Figure 5d). The SSTA in the NINO3 region briefly cools  
385 (Figure 5a) in month 7. At this same time (forecast months 6-8), westerlies prevail from the  
386 western boundary all the way to the dateline. The next downwelling Kelvin wave is initiated in  
387 the west and arrives at the eastern boundary roughly at forecast month 9. As it enters the NINO3  
388 region this downwelling Kelvin wave warms the SSTA. The warmest SSTA fills in to the west  
389 and by month 10 some of the warmest SSTA is located just east of the dateline. Bjerknes  
390 feedback becomes entrenched and westerlies to the west of the SSTA maximum converge with  
391 easterlies to the east (Figure 5c).

392 Careful examination of the equatorial signal and Kelvin/Rossby wave decomposition of  
393 the ocean waves helps to explain the timing and sign of the differences in the mean state in

394     Figure 4a. After 3 month forecasts, downwelling Kelvin waves that are forced by westerlies in  
395     the western Pacific, start to warm the eastern Pacific. After 7 month lead times, the Bjerknes  
396     feedback mechanism begins to lock in leading to enhanced westerlies over the western Pacific  
397     (Figure 5c) and growth of the air-sea coupled mode. The atmospheric impact of including the  
398     interannual forcing in the IO is to impart a large-scale downwelling favorable signal in the  
399     Pacific, increasing the warming in the NINO3 region after the 3 months. By 7 month lead times,  
400     the El Niño signal is enhanced/reinforced due to Bjerknes feedback.

401           To a large part, the previous discussion reinforces the conjecture of [*Annamalai et al.*,  
402     2010] who suggested that the impact of the IO would be to enhance the westerlies along the  
403     equator and amplify an ongoing El Niño. However, examination of the various fields besides  
404     equatorial Hovmöller plots suggests that the initialization and growth of the warming in the  
405     NINO3 region is influenced by off-equatorial factors and by not only zonal but also meridional  
406     wind stress. Therefore, the discussion will now focus on the Pacific basin using plots of the  
407     mean forecast for 3, 5, 7, and 10 month lead times for SSTA, sea level anomaly, curl and  
408     divergence differences for INT\_PAC, INT\_IO minus INT\_PAC, CLIM\_IO results (Figure 7 to  
409     Figure 10, respectively).

410           On the equator, Ekman pumping velocity is undefined (since the Coriolis parameter is in  
411     the denominator). However, near the equator the wind stress divergence can be diagnosed to  
412     infer regions of upwelling or downwelling. By month 3 of the mean forecast, divergence  
413     corresponds to upwelling between 140°E-150°W on the equator and convergence is found  
414     between 140°W-110°W (Figure 7d). Off the equator, downwelling favorable curl (curl <0 in the  
415     Northern Hemisphere and > 0 in the Southern Hemisphere) can be seen west of 140°W generally  
416     within 10° of the equator (Figure 7c). West of 160°W in the far western Pacific downwelling

417 favorable curl off the equator corresponds to positive sea level anomalies off New Guinea  
418 (Figure 7b). This feature is important since it initiates the transition from the upwelling prior to  
419 month 3 across the basin to overall downwelling after that time. In other words, the off-  
420 equatorial curl initializes a downwelling Rossby wave and positive sea level anomaly in the far  
421 western Pacific that soon reflects as a downwelling Kelvin wave that begins the eventual  
422 transition to warm SSTA in the NINO3 region by month 7. This is an instance where the off-  
423 equatorial signal (a downwelling Rossby wave) contributes to converting upwelling to  
424 downwelling along the equator and so features prominently in ENSO predictability.

425 Unfortunately, this downwelling in the west is not well represented by the Kelvin/Rossby  
426 decomposition plot (Figure 6) since it lies west of 160°E which is the western extent of the land-  
427 free symmetric box that is required by this decomposition analysis. However, the subsequent  
428 downwelling Kelvin wave (spawned from the reflected Rossby wave) in the far west starting in  
429 month 4 is well diagnosed.

430 To the east, a pair of upwelling-favorable (negative in the Northern Hemisphere positive  
431 in the Southern Hemisphere) curl patches are located within 15°S-10°N between 140°W-110°W  
432 (Figure 7c). This feature corresponds with a pair of negative sea level anomalies centered at  
433 5°N and 12°S at 130°W and is identified as an upwelling Rossby wave in the Kelvin/Rossby  
434 diagnosis in Figure 6b. East of 160°W, an upwelling Rossby wave at 140°W acts to shoal the  
435 thermocline at 5°N and 10°S reshaping the meridional gradient to help focus the downwelling  
436 Kelvin wave train along the equator coming later in the average forecast.

437 In summary, downwelling Rossby waves forced by wind stress curl off the equator in the  
438 far western Pacific reflect to downwelling Kelvin waves eventually transitioning the NINO3

439 region to warming. The upwelling Rossby wave at 140°W at month 3 shapes the meridional  
440 gradient to focus intensification on the equator.

441 By month 5 the downwelling Rossby wave hitting the western boundary in month 3 has  
442 reflected into a downwelling Kelvin wave and this wave has propagated eastward across the  
443 Pacific as far as ~140°W (Figure 8b and Figure 6a). The effects of this downwelling Kelvin  
444 wave are demonstrated by positive sea level and SST anomaly throughout the waveguide (+/- 2°)  
445 across the entire Pacific (Figure 8a). The upwelling features in Figure 8c are echoed in negative  
446 sea level at 5°N and 10°S at 145°W (Figure 8b). The NINO3 region is warming and SSTA is  
447 largest at about 120°W on the equator. It is also interesting to note that the warmest SSTA is just  
448 south of the equator whereas the sea level anomaly maximum is centered on the equator.  
449 Convergence found on the equator and positive curl and downwelling just to the south (5°S-0°S,  
450 140°W-110°W) coincide with maximum SSTA. Going from 5°N to 12°S along 130°W winds  
451 are starting northerly recurring to northwesterlies just south of the equator. West of the dateline  
452 and south of 5°S, pervasive positive curl (downwelling favorable) is collocated with positive sea  
453 level anomaly against New Guinea and Australia coasts. To the north of the equator, positive  
454 curl and upwelling are found with negative sea level west of 150°E off the Philippines. Thus the  
455 southeasterlies to the south recurring to southwesterlies north of the equator in the far western  
456 Pacific act to deepen and shoal sea level, respectively. To reiterate, not only are the equatorial  
457 signals important for the diagnosing the impact of the IO on ENSO, but the off-equatorial  
458 impacts such as oceanic Rossby wave formation and propagation are also important.

459 By month 7 the second Kelvin wave has reflected at the eastern boundary as a  
460 downwelling Rossby wave as evident by positive sea level at 10°N, 5°S at 120°W (Figure 9b and  
461 Figure 6b). Another positive sea level and SSTA maximum is centered on the equator at

462 ~170°W (Figure 9a, b). Equatorial westerlies, best demonstrated by the westerly wind burst in  
463 Figure 5c that extends from the western boundary to 160°E (note the  $2 \times 10^{-3}$  N/m<sup>2</sup> contour), force  
464 this downwelling Kelvin wave. To the north, downwelling curl corresponds to positive sea level  
465 and to the south negative sea level is collocated with upwelling favorable wind stress curl at  
466 10°N, 10°S at ~150°W, respectively. Off the equator, west of 160°E the curl is positive to the  
467 north and this forces upwelling 0-10°N and negative sea level. It is also interesting to note that  
468 upwelling curl within 5° of the equator in the NINO3 region (particularly at 120°W) is causing  
469 weak upwelling and cold SSTA at 5°N driving the warmest SST south of the equator (Figure 9a).

470 By month 10 the Bjerknes feedback has locked in (Figure 10). SSTA is positive  
471 throughout the equatorial band between 160°E to the eastern boundary. The negative sea level  
472 horseshoe pattern is evident off the equator in the west and positive values east of 160°E near the  
473 equator typically associated with a mature El Niño. On the equator, winds are diverging between  
474 150°E-175°E and converging to the east of there between 150°W-100°W. To the east of 150°W  
475 and off the equator, the curl and sea level are in good agreement. At 10°N, 150°W, downwelling  
476 curl corresponds with positive sea level anomaly. At 2°N, 135°W positive curl overlays with a  
477 small region of negative sea level. Just south of the equator at 135°W, downwelling curl  
478 coincides with a maximum of sea level and SSTA. Further to the south at 10°S and 140°W  
479 upwelling curl and negative sea level coincide. Thus the pattern of upwelling/downwelling curl  
480 of the wind maintains the meridional sea level gradient east of 160°W. Off the equator west of  
481 160°W, upwelling curl is acting to reinforce the negative sea level off the Philippines and off the  
482 coast of New Guinea and Australia. To summarize, the mean forecast by 10 month lead times  
483 shows winds that are primarily diverging away from the equator west of the dateline  
484 (southwesterlies to the north and northwesterlies to the south of the equator) and converging

485 towards the equator east of the dateline (with northeasterlies north of the equator slowing and  
486 turning towards northwesterlies at the equator). These diagnostics of the average coupled  
487 forecast reveals that the response of the ENSO system in the Pacific is more complicated than  
488 simply triggering a westerly wind burst in the western Pacific on the equator and setting off  
489 downwelling Kelvin waves eventually warming the NINO3 region as assumed by [Annamalai *et*  
490 *al.*, 2010] and others. Our diagnosis suggests that the atmospheric response is more complicated  
491 than previously thought, and a previously unaccounted-for significant signal corresponds to  
492 strong easterlies south of 15°S and between 0°N to 20°N.

493 Our results may be usefully contrasted with previous work employing simpler  
494 atmospheric models and idealized surface forcing. Similar to previous work, there are weak  
495 westerlies near the equator (10°S-0°N) across the entire Pacific. These relatively weak winds we  
496 simulate near the equator match those of [Annamalai *et al.*, 2005] who used a simple linear  
497 atmospheric model (a moist linear baroclinic model – LBM of [Watanabe and Jin, 2003]) to  
498 show that the atmospheric Kelvin wave of the western dipole of the IODZM cancels that of the  
499 eastern dipole (their Figures 8b, 10d). However, our results show the importance of not only the  
500 near-equatorial winds but also the off-equatorial zonal and meridional winds for the diagnosis of  
501 the IO SSTA teleconnections to Pacific ENSO (Figure 2a).

502 The off-equatorial easterlies represented in Figure 2a are a prominent feature but are  
503 lacking in previous studies (e.g. [Wu and Kirtman, 2004] Figure 7d, [Annamalai *et al.*, 2010]  
504 Figure 7d). There are several reasons why the simple atmospheric models that were used to  
505 highlight the IO atmospheric teleconnections to the Pacific ([Wu and Kirtman, 2004] and  
506 [Annamalai *et al.*, 2010]) might lack the off-equatorial easterlies simulated in SPEEDY. In  
507 previous results, the IO SST field is idealized in some way or another. Either the 1<sup>st</sup> EOF of the

coupled model results or the SST differences with and without IODZM for El Niño is utilized to simplify the SST forcing. In addition, these models have been linearized about different mean states for specific seasons (JJAS and MJ, respectively) so the seasonal cycle remaining in SPEEDY may play a role in forming the off-equatorial easterlies. When we limit the SSTA forcing in the IO to just the 1<sup>st</sup> EOF of the simulated SSTA (not shown but a similar pattern as [Wu and Kirtman, 2004] Figure 7a for the IO) for the forced SPEEDY AGCM, the anomalous westerlies near the equator are enhanced: the atmospheric Kelvin wave is present as in previous research but the easterlies off the equator remain.

The lack of a strong signal off the equator for the LBM results of the previous authors is surprising considering the results of [Watanabe and Jin, 2003]. They used a similar model (LBM) as previous authors and forced it with El Niño minus La Niña observed SSTA limited to the IO region. Their Figure 8c indicates that a basin-scale cooling in the IO (their M3 region) results in a positive precipitation response symmetric within 15° of the equator that is centered at 140°E. West of the dateline, the 850 mb streamfunction response to this heating shows nearly collocated cyclonic flow and easterlies between 10°N-35°N, westerlies for 5°N-10°S, and easterlies between 15°S-30°S west of the dateline, which are broadly similar to our results. On the other hand, our precipitation results have this maximum centered to the east, at roughly 160°W (Figure 2c), so this displacement of the precipitation heating might explain the elongated off-equatorial easterlies found in the SPEEDY results (Figure 2a).

Another potential difference between previously reported results and the current wind results is the amplitude and location of the precipitation anomalies in the Pacific. For example, [Annamalai *et al.*, 2010] shows (their Figure 2b) the strong positive precipitation anomalies centered at 10°S and 5°N centered at 180°, roughly similar to our results. However, for these

531 previous results there is also a strong negative anomaly with similar zonal extent and amplitude  
532 to the west, centered at 150°E that may act to offset any off-equatorial signal in the winds. Our  
533 precipitation results (Figure 2c) show that there are no such offsetting precipitation anomalies to  
534 the west of the main positive values located between 160°E to 160°W centered at 10°S and 5°N.  
535 Therefore, off-equatorial easterlies are not opposed by westerlies for the SPEEDY results.

536 The last and most likely potential reason for off-equatorial easterlies may be the  
537 convective scheme within the SPEEDY results. [Kim *et al.*, 2008] show that implementation of  
538 CMT leads to enhanced off-equatorial precipitation (roughly 5°-15° off the equator) and  
539 decreased precipitation between 5°S-5°N. The wind response to implementation of CMT is  
540 increased 850 mb westerlies between 10°S-10°N and also easterlies poleward of the enhanced  
541 precipitation. However, these results are only valid west of 150°W for the December - February  
542 climatological forcing used for the [Kim *et al.*, 2008] example. A fundamental concept of CMT  
543 is that upper atmosphere momentum is transported to the surface via downdrafts around  
544 convection. In our example, the generally enhanced precipitation (Figure 2c) between 15°S-5°N  
545 drags westerly momentum from upper branch of the Walker circulation to the surface (Figure  
546 2a). At the same time, weaker precipitation for the coupled IO with respect to the decoupled IO  
547 does the opposite leaving enhanced easterlies between 5°N-20°N and south of 15°S. Thus,  
548 implementation of CMT within SPEEDY, but not within any of the linear model results, may  
549 also contribute to the off-equatorial easterlies found in the SPEEDY results. Although there are  
550 multiple potential reasons for differences between the nonlinear LBM and SPEEDY atmospheric  
551 results, exploring differences further is beyond the scope of the current paper.

552 The combined impact of the zonal and meridional winds in the Pacific on the ocean can  
553 be conveniently summarized by diagnosing the differences of the SPEEDY experiments using

curl and divergence of the wind stress. On the equator, surface convergence of the wind leads to convergence of the surface currents, downwelling in the ocean, a deepening of the thermocline, and an increase in sea level. The divergence of the atmospheric teleconnections is presented in Figure 2f and this shows pervasive downwelling favorable winds all along the entire equator. Off the equator, the curl can be used to estimate the sense of Ekman pumping velocity as a measure of upwelling or downwelling. Figure 2e shows that upwelling favorable winds (positive in the Northern Hemisphere and negative in the Southern Hemisphere) are predominant between 15°S to 10°N in the Pacific. However, the curl just to the south of the equator between 160°E-140°W is positive indicating a narrow band of downwelling favorable curl. North of ~10°N and in the southwest Pacific (off Australia) downwelling curl is also prevalent.

To summarize differences between the present study and prior work, forced experimental minus control atmospheric simulations produce strong easterly differences south of 15°S and between the equator and 20°N in the Pacific, with weak westerly differences near the equator between 10°S and the equator. For the meridional component, winds converge towards 5°S especially over the eastern half of the basin with abundant precipitation in the eastern Pacific cold tongue region near the equator. In addition, differences show strong positive precipitation anomalies in the central Pacific. Convergence along the equator indicates that there is pervasive downwelling favorable conditions present at initialization of the coupled system along the equator. However, off the equator between 15°S-10°N the prevailing curl indicates that IO SSTA is generally forcing upwelling in this region. As [Annamalai *et al.*, 2005] noted, the weak winds within the waveguide may allow nascent El Niño/La Niña events to grow unencumbered.

575

576     **6 Summary and Conclusions**

577         Our results suggest that additional validated forecast skill is available for operational  
578         ENSO forecasting improvements by including IO forcing and realistically nonlinear modelling  
579         of the response of the coupled Indo-Pacific ocean atmosphere system. A key potential source  
580         that we have identified in this study is the impact of atmospheric teleconnections originating  
581         from the IO. Coupled experiments described herein that are initialized with the full observed  
582         SST forcing and utilize a nonlinear atmosphere indicate that our atmospheric response in the  
583         Pacific to interannual IO forcing includes weak westerly winds equatorward of 10°S, enhanced  
584         off-equatorial trade winds and strengthened easterlies between 30°S to 15°S and the equator to  
585         25°N. The differences between the previous linear atmospheric model and our AGCM  
586         (SPEEDY) results may be due to either simplification of IO forcing, displacement of  
587         precipitation (and heating) to the east with no compensating anomaly, or most likely, the  
588         convective momentum transport in SPEEDY. These off-equatorial winds have profound impact  
589         in that they generate wind stress curl that act to amplify the oceanic Rossby wave signal which  
590         eventually impact the eastern Pacific by way of reflected Kelvin waves.

591         Differences between coupled experiments show that including the impact of interannual  
592         teleconnections from the IO have significantly higher ENSO correlation (exceeding the 95%  
593         significance level from 3-9 months) and lower RMS validation statistics. The reason for this is a  
594         combination of equatorial and off-equatorial coupling that eventually warms the NINO3 region.  
595         Early in the forecast period, prior to 3 month lead times, equatorial upwelling in the western  
596         Pacific weakly cools the NINO3 region via propagation of upwelling Kelvin waves. After that  
597         time, off-equatorial downwelling favorable curl in the western Pacific helps to amplify the  
598         transition from cooling to warming in the NINO3 region by way of reflected downwelling  
599         Rossby to downwelling Kelvin waves. Downwelling Kelvin waves, amplified by equatorial

600 convergence, warm the eastern Pacific and improve correlation validation after 3 month lead  
601 times with respect to observations. The improvement in correlation peaks at 7 months which  
602 corresponds with the time it takes for the transmission of the reflected downwelling Rossby wave  
603 to reflect into the downwelling Kelvin wave then to propagate across the Pacific into the NINO3  
604 region. Therefore, a main conclusion from these results is that the interannual variability of IO  
605 SST forcing is responsible for overall somewhat lagged widespread downwelling in the Pacific,  
606 assisted by off-equatorial curl, leading to warmer NINO3 SST anomaly and improved validation  
607 after 3 month lead times.

608 Currently ENSO forecast discussions (see [http://origin.cpc.ncep.noaa.gov/  
609 products/GODAS/ocean\\_briefing\\_gif/global\\_ocean\\_monitoring\\_current.ppt](http://origin.cpc.ncep.noaa.gov/products/GODAS/ocean_briefing_gif/global_ocean_monitoring_current.ppt)) include  
610 descriptions of large-scale ocean waves present in the initialization of coupled forecasts.  
611 However, these discussions only assess the state of the oceanic Kelvin wave (using the Ocean  
612 Kelvin Wave Index, an extended EOF technique) and this would suggest a lack of emphasis on  
613 off-equatorial processes in coupled model initialization. On the contrary, the results of the  
614 impact of the teleconnections from the IO to the Pacific presented herein demonstrate the  
615 significance of the off-equatorial processes that generate oceanic Rossby waves. Therefore, we  
616 recommend that the impact of the Rossby waves on ENSO should be included in forecast  
617 discussions. We have shown that the impact of the IO atmospheric teleconnections to ENSO  
618 significantly improve coupled forecasts from 3-9 month lead times, so both upstream IO  
619 influences and off-equatorial processes should be considered/included in ENSO forecasting  
620 systems.

621     **Acknowledgments**

622         This work was completed as part of the Accomplished Scientist Ph. D. Program at the  
623         University of Maryland. We would like to thank Dr. Fred Kucharski who provided all software  
624         and guidance on implementing SPEEDY into our coupled model. The SPEEDY model is freely  
625         available and can be downloaded from <http://users.ictp.it/~kucharsk/speedy-net.html>. Dr. Travis  
626         Sluka helped with early questions about CMT and SPEEDY and Dr. Hugo Berbery provided his  
627         expertise on atmospheric model questions. We gratefully acknowledge the comments from the  
628         anonymous reviewers who helped to improve this manuscript. We acknowledge NASA for  
629         supporting much of the research contained in this paper (NASA Grants NNX13AM61G,  
630         NNX09AF41G, and NNX16AH62G). We would also thank everyone involved with  
631         development of the ocean model particularly James Beauchamp and Joaquim Ballabrera-Poy.  
632         The source code for the ocean model used in this study is freely available. Both the data and  
633         input files necessary to reproduce the experiments with our OGCM are available from the  
634         authors upon request ([ehackert@essic.umd.edu](mailto:ehackert@essic.umd.edu)). All observational data for this paper is properly  
635         cited and referred to in the reference list.

636 **References**

- 637 Adler, R. F., et al. (2003), The version-2 global precipitation climatology project (GPCP)  
638 monthly precipitation analysis (1979-present), *Journal of Hydrometeorology*, 4(6), 1147-  
639 1167.
- 640 Alexander, M. A., I. Blade, M. Newman, J. R. Lanzante, N. C. Lau, and J. D. Scott (2002), The  
641 atmospheric bridge: The influence of ENSO teleconnections on air-sea interaction over  
642 the global oceans, *Journal of Climate*, 15(16), 2205-2231.
- 643 Annamalai, H., S. Kida, and J. Hafner (2010), Potential Impact of the Tropical Indian Ocean-  
644 Indonesian Seas on El Niño Characteristics, *Journal of Climate*, 23(14), 3933-3952.
- 645 Annamalai, H., S. P. Xie, J. P. McCreary, and R. Murtugudde (2005), Impact of Indian Ocean  
646 sea surface temperature on developing El Niño, *Journal of Climate*, 18(2), 302-319.
- 647 Antonov, J. I., D. Seidov, T. P. Boyer, R. A. Locarnini, A. V. Mishonov, H. E. Garcia, O. K.  
648 Baranova, M. M. Zweng, and D. R. Johnson (2010), World Ocean Atlas 2009, Volume 2:  
649 Salinity., in *NOAA Atlas NESDIS 69*, edited by Secondary Antonov, J. I., D.  
650 Seidov, T. P. Boyer, R. A. Locarnini, A. V. Mishonov, H. E. Garcia, O. K. Baranova, M.  
651 M. Zweng, and D. R. Johnson, p. 184 pp., U.S. Government Printing Office, Washington,  
652 D.C.
- 653 Behringer, D. (2007), The Global Ocean Data Assimilation System (GODAS) at NCEP, paper  
654 presented at 11th Symp. on Integrated Observing and Assimilation Systems for  
655 Atmosphere, Oceans and Land Surface, American Meteorological Society San Antonio,  
656 TX [Available online at <http://ams.confex.com/ams/pdfpapers/119541.pdf>].
- 657 Bracco, A., F. Kucharski, F. Molteni, W. Hazeleger, and C. Severijns (2005), Internal and forced  
658 modes of variability in the Indian Ocean, *Geophysical Research Letters*, 32(12).
- 659 Chen, D., L. M. Rothstein, and A. J. Busalacchi (1994), A Hybrid Vertical Mixing Scheme and  
660 Its Application to Tropical Ocean Models, *Journal of Physical Oceanography*, 24(10),  
661 2156-2179.
- 662 Delcroix, T., J. P. Boulanger, F. Masia, and C. Menkes (1994), Geosat-Derived Sea-Level and  
663 Surface Current Anomalies in the Equatorial Pacific During the 1986-1989 El-Niño and  
664 La-Niña, *Journal of Geophysical Research-Oceans*, 99(C12), 25093-25107.
- 665 ECMWF (1994), The description of the ECMWF/WCRP Level III-A Global Atmospheric Data  
666 Archive, *Tech. Attach. Rep.*, 72 pp. pp, European Centre for Medium-Range Weather  
667 Forecasts, Reading, England, U.K.
- 668 Gent, P. R., and M. A. Cane (1989), A Reduced Gravity, Primitive Equation Model of the Upper  
669 Equatorial Ocean, *Journal of Computational Physics*, 81(2), 444-480.

- 670 Gibson, J. K., P. Kallberg, S. Uppala, F. Hernandez, R. Nomura, and Y. Serrano (1997),  
671 ECMWF re-analysis. *Rep.*, European Centre for Medium-Range Weather Forecasts,  
672 Reading (UK).
- 673 Glantz, M. H. (2001), *Currents of Change: El Nino and La Nina Impacts on Climate and*  
674 *Society*, 252 pp., Cambridge University Press, Cambridge, UK.
- 675 Griffies, S. M., M. J. Harrison, R. C. Pacanowski, and A. Rosati (2004), Technical Guide to  
676 MOM4, in *GFDL Ocean Group Technical Report 5* edited by Secondary  
677 Griffies, S. M., M. J. Harrison, R. C. Pacanowski, and A. Rosati, p. 337, GFDL GFDL  
678 Princeton, NJ [Available online at [www.gfdl.noaa.gov/~fms](http://www.gfdl.noaa.gov/~fms)].
- 679 Hackert, E., A. Busalacchi, and J. Ballabrera-Poy (2014), Impact of Aquarius sea surface salinity  
680 observations on coupled forecasts for the tropical Indo-Pacific Ocean, *Journal of*  
681 *Geophysical Research, Oceans*, 119(doi: 10.1002/2013JC009697).
- 682 Hackert, E., J. Ballabrera-Poy, A. J. Busalacchi, R. H. Zhang, and R. Murtugudde (2007),  
683 Comparison between 1997 and 2002 El Nino events: Role of initial state versus forcing,  
684 *Journal of Geophysical Research-Oceans*, 112(C1).
- 685 Hackert, E. C., A. J. Busalacchi, and R. Murtugudde (2001), A wind comparison study using an  
686 ocean general circulation model for the 1999-1998 El Niño, *Journal of Geophysical*  
687 *Research-Oceans*, 106(C2), 2345-2362.
- 688 Horel, J. D., and J. M. Wallace (1981), PLANETARY-SCALE ATMOSPHERIC  
689 PHENOMENA ASSOCIATED WITH THE SOUTHERN OSCILLATION, *Monthly*  
690 *Weather Review*, 109(4), 813-829.
- 691 Huang, R. X. (1993), Real Fresh-Water Flux as a Natural Boundary-Condition for the Salinity  
692 Balance and Thermohaline Circulation Forced by Evaporation and Precipitation, *Journal*  
693 *of Physical Oceanography*, 23(11), 2428-2446.
- 694 Kalnay, E., et al. (1996), The NCEP/NCAR 40-year reanalysis project, *Bulletin of the American*  
695 *Meteorological Society*, 77(3), 437-471.
- 696 Kessler, W. S., M. J. McPhaden, and K. M. Weickmann (1995), Forcing of Intraseasonal Kelvin  
697 Waves in the Equatorial Pacific, *Journal of Geophysical Research-Oceans*, 100(C6),  
698 10613-10631.
- 699 Kim, D., J. S. Kug, I. S. Kang, F. F. Jin, and A. T. Wittenberg (2008), Tropical Pacific impacts  
700 of convective momentum transport in the SNU coupled GCM, *Climate Dynamics*, 31(2-  
701 3), 213-226.
- 702 Kraus, E. B., and J. S. Turner (1967), A One-Dimensional Model of Seasonal Thermocline .2.  
703 General Theory and Its Consequences, *Tellus*, 19(1), 98-&.
- 704 Kroeger, J., and F. Kucharski (2011), Sensitivity of ENSO characteristics to a new interactive  
705 flux correction scheme in a coupled GCM, *Climate Dynamics*, 36(1-2), 119-137.

- 706 Kucharski, F., F. Molteni, and J. H. Yoo (2006), SST forcing of decadal Indian Monsoon rainfall  
707 variability, *Geophysical Research Letters*, 33(3).
- 708 Kucharski, F., I. S. Kang, R. Farneti, and L. Feudale (2011), Tropical Pacific response to 20th  
709 century Atlantic warming, *Geophysical Research Letters*, 38.
- 710 Kucharski, F., F. Molteni, M. P. King, R. Farneti, I.-S. Kang, and L. Feudale (2013), On the  
711 Need of Intermediate Complexity General Circulation Models A "SPEEDY" Example,  
712 *Bulletin of the American Meteorological Society*, 94(1), 25-30.
- 713 Lau, N. C., and M. J. Nath (2003), Atmosphere-ocean variations in the Indo-Pacific sector during  
714 ENSO episodes, *Journal of Climate*, 16(1), 3-20.
- 715 Locarnini, R. A., A. V. Mishonov, J. I. Antonov, T. P. Boyer, H. E. Garcia, O. K. Baranova, M.  
716 M. Zweng, and D. R. Johnson (2010), World Ocean Atlas 2009, Volume 1: Temperature,  
717 NOAA Atlas NESDIS 68, edited by Secondary Locarnini, R. A., A. V.  
718 Mishonov, J. I. Antonov, T. P. Boyer, H. E. Garcia, O. K. Baranova, M. M. Zweng, and  
719 D. R. Johnson, p. 184 pp., U.S. Government Printing Office, Washington, D.C.
- 720 McPhaden, M. J. (2015), Playing hide and seek with El Nino, *Nature Clim. Change*, 5(9), 791-  
721 795.
- 722 Menkes, C. E., M. Lengaigne, J. Vialard, M. Puy, P. Marchesiello, S. Cravatte, and G. Cambon  
723 (2014), About the role of Westerly Wind Events in the possible development of an El  
724 Nino in 2014, *Geophysical Research Letters*, 41(18), 6476-6483.
- 725 Min, Q., J. Su, R. Zhang, and X. Rong (2015), What hindered the El Nino pattern in 2014?,  
726 *Geophysical Research Letters*, 42(16), 6762-6770.
- 727 Molteni, F. (2003), Atmospheric simulations using a GCM with simplified physical  
728 parametrizations. I: model climatology and variability in multi-decadal experiments,  
729 *Climate Dynamics*, 20(2-3), 175-191.
- 730 Murtugudde, R., and A. J. Busalacchi (1998), Salinity effects in a tropical ocean model, *Journal*  
731 *of Geophysical Research-Oceans*, 103(C2), 3283-3300.
- 732 Murtugudde, R., R. Seager, and A. Busalacchi (1996), Simulation of the tropical oceans with an  
733 ocean GCM coupled to an atmospheric mixed-layer model, *Journal of Climate*, 9(8),  
734 1795-1815.
- 735 Murtugudde, R., A. J. Busalacchi, and J. Beauchamp (1998), Seasonal-to-interannual effects of  
736 the Indonesian Throughflow on the tropical Indo-Pacific Basin, *Journal of Geophysical*  
737 *Research-Oceans*, 103(C10), 21425-21441.
- 738 National Academies of Sciences, E., and Medicine (2016), *Next Generation Earth System*  
739 *Prediction: Strategies for Subseasonal to Seasonal Forecasts*, 290 pp., The National  
740 Academies Press, Washington, DC.

- 741 National Research Council (2010), *Assessment of intraseasonal to interannual climate prediction*  
742 *and predictability*, National Academies Press, Washington, D.C. :.
- 743 Picaut, J., and R. Tournier (1991), MONITORING THE 1979-1985 EQUATORIAL PACIFIC  
744 CURRENT TRANSPORTS WITH EXPENDABLE BATHYTHERMOGRAPH DATA,  
745 *Journal of Geophysical Research: Planets*, 96, 3263-3277.
- 746 Price, J. F., R. A. Weller, and R. Pinkel (1986), Diurnal Cycling - Observations and Models of  
747 the Upper Ocean Response to Diurnal Heating, Cooling, and Wind Mixing, *Journal of*  
748 *Geophysical Research-Oceans*, 91(C7), 8411-8427.
- 749 Quenouille, M. H. (1952), *Associated measurements*, 242 pp., Buterworths, London.
- 750 Rayner, N. A., D. E. Parker, E. B. Horton, C. K. Folland, L. V. Alexander, D. P. Rowell, E. C.  
751 Kent, and A. Kaplan (2003), Global analyses of sea surface temperature, sea ice, and  
752 night marine air temperature since the late nineteenth century, *Journal of Geophysical*  
753 *Research-Atmospheres*, 108(D14).
- 754 Reynolds, R. W., N. A. Rayner, T. M. Smith, D. C. Stokes, and W. Q. Wang (2002), An  
755 improved in situ and satellite SST analysis for climate, *Journal of Climate*, 15(13), 1609-  
756 1625.
- 757 Rossow, W. B., and R. A. Schiffer (1991), Isccp Cloud Data Products, *Bulletin of the American*  
758 *Meteorological Society*, 72(1), 2-20.
- 759 Saha, S., et al. (2014), The NCEP Climate Forecast System Version 2, *Journal of Climate*, 27(6),  
760 2185-2208.
- 761 Saha, S., et al. (2010), THE NCEP CLIMATE FORECAST SYSTEM REANALYSIS, *Bulletin*  
762 *of the American Meteorological Society*, 91(8), 1015-1057.
- 763 Santoso, A., M. H. England, and W. Cai (2012), Impact of Indo-Pacific Feedback Interactions on  
764 ENSO Dynamics Diagnosed Using Ensemble Climate Simulations, *Journal of Climate*,  
765 25(21), 7743-7763.
- 766 Steiger, J. H. (1980), TESTS FOR COMPARING ELEMENTS OF A CORRELATION  
767 MATRIX, *Psychological Bulletin*, 87(2), 245-251.
- 768 Uehara, H., A. A. Kruts, H. Mitsudera, T. Nakamura, Y. N. Volkov, and M. Wakatsuchi (2014),  
769 Remotely propagating salinity anomaly varies the source of North Pacific ventilation,  
770 *Progress in Oceanography*, 126, 80-97.
- 771 Watanabe, M., and F. F. Jin (2003), A moist linear baroclinic model: Coupled dynamical-  
772 convective response to El Nino, *Journal of Climate*, 16(8), 1121-1139.
- 773 Wu, R. G., and B. P. Kirtman (2004), Understanding the impacts of the Indian Ocean on ENSO  
774 variability in a coupled GCM, *Journal of Climate*, 17(20), 4019-4031.

- 775 Xie, P. P., and P. A. Arkin (1998), Global monthly precipitation estimates from satellite-  
776 observed outgoing longwave radiation, *Journal of Climate*, 11(2), 137-164.
- 777 Yu, J. Y., C. R. Mechoso, J. C. McWilliams, and A. Arakawa (2002), Impacts of the Indian  
778 Ocean on the ENSO cycle, *Geophysical Research Letters*, 29(8).
- 779 Zhou, L., R. B. Neale, M. Jochum, and R. Murtugudde (2012), Improved Madden-Julian  
780 Oscillations with Improved Physics: The Impact of Modified Convection  
781 Parameterizations, *Journal of Climate*, 25(4), 1116-1136.
- 782
- 783
- 784

785 **Figure 1:** Validation of the SPEEDY coupled model. Our Indo-Pacific SPEEDY coupled  
786 model (red) is a) correlated and b) RMSD against observed NINO3 SSTA for Jan. 1993-Mar.  
787 2011. CFSRR coupled model results (black) are included to put our coupled results into the  
788 context of a more widely known coupled model. Individual correlations exceed the 95%  
789 significance out to 8.3 (35) and 10 months (34) (effective degrees of freedom) for red and black  
790 lines, respectively. Observation persistence is indicated by the thin black dotted line. This  
791 version of the SPEEDY coupled model assimilates all available satellite (sea level, SST) and in  
792 situ information (sea surface salinity and subsurface temperature and salinity) using the data  
793 assimilation technique described in [Hackert *et al.*, 2014].

794 **Figure 2:** Impact of interannual IO SST forcing. Differences between two sets of SPEEDY  
795 atmosphere-only experiments for a) zonal, b) meridional wind stress, c) precipitation, d) vector  
796 representation of a) and b), e) curl and f) divergence of the wind stress. Differences are full SST  
797 anomaly forcing over the Indo-Pacific region (i.e. INT\_PAC, INT\_IO) minus the experiment that  
798 uses climatological seasonal cycle forcing over the IO (INT\_PAC, CLIM\_IO). Letters “U” and  
799 “D” represent regions of upwelling and downwelling favorable winds and absolute values greater  
800 than  $3.3 \times 10^{-3} \text{ N/m}^2$ ,  $2.7 \times 10^{-3} \text{ N/m}^2$ ,  $13.2 \text{ mm/mon}$ ,  $0.53 \times 10^{-9} \text{ N/m}^3$ ,  $0.35 \times 10^{-9} \text{ N/m}^3$  are  
801 significant at the 95% level for a), b) c), e), and f), respectively.

802 **Figure 3:** Impact of IO interannual forcing on coupled NINO3 SST results. Validation statistics  
803 for a) correlation and b) RMS differences between coupled experiments with full atmospheric  
804 coupling (i.e. INT\_PAC, INT\_IO) in red and interannual coupling in the Pacific and  
805 climatological forcing in the IO (i.e. INT\_PAC, CLIM\_IO) in blue. The coupled experiments are  
806 validated against observed NINO3 SST anomaly for 1993 to 2014. Individual correlations  
807 exceed the 95% significance out to 8 (43) and 5.8 months (41) (effective degrees of freedom) for  
808 red and blue lines, respectively. The thick black line on the top x-axis shows where the red line  
809 is significantly larger than the blue line using the Steiger-Z test.

810 **Figure 4:** Mean and variability of NINO3 SST for impact of interannual IO SST forcing. Plots  
811 showing the NINO3 SST a) mean forecast and b) variability for INT\_PAC, INT\_IO (red) and  
812 INT\_PAC, CLIM\_IO (blue) for all forecasts from 1993-2014.

813 **Figure 5:** Hovmöller plots of impact of interannual IO SST forcing. Plots showing the mean  
814 temporal evolution of the impact of IO atmospheric coupling using longitude versus lead time (in  
815 months) averaged between  $2^\circ\text{N}$  and  $2^\circ\text{S}$  for a) SST, b) sea level (SL), c) zonal wind stress, and d)  
816 zonal currents. The mean is taken for the average forecast differences, INT\_PAC, INT\_IO  
817 minus INT\_PAC, CLIM\_IO, over all months from 1993 to 2014.

818 **Figure 6:** Kelvin/Rossby wave decomposition of interannual IO SST forcing. Longitude versus  
819 time distribution of the equatorial (a) Kelvin and (b) the first meridional mode of equatorial  
820 Rossby waves through their signature in zonal surface current deduced from the average forecast  
821 SL differences, (INT\_PAC, INT\_IO) – (INT\_PAC, CLIM\_IO). In order to follow possible wave  
822 reflections on the western (WB) and eastern (EB) boundaries, the Rossby panel (b) is inverted  
823 and the Kelvin wave pattern is repeated (c). The color scale for the Rossby panel is also inverted  
824 since reflection on meridional boundaries results in zonal currents of opposite sign. Solid lines  
825 (downwelling) and dashed lines (upwelling) represent theoretical wave speeds for Kelvin  
826 ( $2.5 \text{ m/s}$ ) and Rossby waves ( $-0.8 \text{ m/s}$  or  $\sim 5 \text{ months}$  to cross this Pacific basin at  $5^\circ\text{N}$ ) on each plot.

827   **Figure 7:** Average 3 month forecast INT\_PAC, INT\_IO - INT\_PAC, CLIM\_IO. Average  
828   forecast values for month 3 for a) SST, b) sea level, c) curl of the wind stress (color) and wind  
829   stress (vector), and d) divergence of the wind stress (color) and wind stress (vector). The scale  
830   of the vector plot is indicated in the bottom left of the panel. For the reader's convenience,  
831   regions of upwelling and downwelling are marked by letters U and D, respectively.

832   **Figure 8:** Average 5 month forecast INT\_PAC, INT\_IO - INT\_PAC, CLIM\_IO. Same as  
833   previous but for 5 month average forecasts.

834   **Figure 9:** Average 7 month forecast INT\_PAC, INT\_IO - INT\_PAC, CLIM\_IO. Same as  
835   previous but for 7 month lead forecast mean.

836   **Figure 10:** Average 10 month forecast INT\_PAC, INT\_IO - INT\_PAC, CLIM\_IO. Same as  
837   previous but for 10 month forecast mean.  
838

Experiment Name	Period	Model Geometry (Atmosphere/Ocean)	Indo-Pacific Forcing
INT_PAC, INT_IO	1993-2014	Global/Indo-Pacific	Interannual SSTA forcing for Pacific and IO
INT_PAC, CLIM_IO	1993-2014	Global/Indo-Pacific	Interannual SSTA forcing for Pacific, climatological seasonal cycle SST for IO

839 **Table 1:** Experiment description for impact of interannual IO SST forcing. The far left column  
 840 describes the experiments, “INT” and “CLIM” stand for interannual and climatological forcing  
 841 and “PAC” and “IO” stand for Pacific ( $30^{\circ}\text{S}$ - $30^{\circ}\text{N}$ ,  $130^{\circ}\text{E}$ - $70^{\circ}\text{W}$ ) and Indian Oceans ( $30^{\circ}\text{S}$ - $30^{\circ}\text{N}$ ,  
 842  $30^{\circ}\text{E}$ - $129^{\circ}\text{E}$ ), respectively. The far right column describes the SST anomaly forcing (SSTA) for  
 843 the Indo-Pacific region. In order to isolate the impact of the IO, differences between  
 844 INT\_PAC, INT\_IO – INT\_PAC, CLIM\_IO are presented. Note that SSTA are formulated with  
 845 respect to the 1983-2014 mean seasonal cycle using [Reynolds et al., 2002] OI SST.  
 846

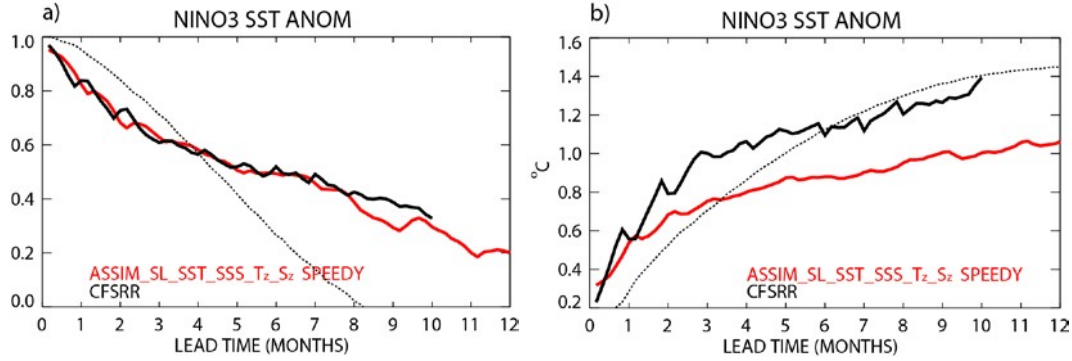


**Figure 1:** Validation of the SPEEDY coupled model. Our Indo-Pacific SPEEDY coupled model (red) is a) correlated and b) RMSD against observed NINO3 SSTA for Jan. 1993-Mar. 2011. CFSRR coupled model results (black) are included to put our coupled results into the context of a more widely known coupled model. Individual correlations exceed the 95% significance out to 8.3 (35) and 10 months (34) (effective degrees of freedom) for red and black lines, respectively. Observation persistence is indicated by the thin black dotted line. This version of the SPEEDY coupled model assimilates all available satellite (sea level, SST) and in situ information (sea surface salinity and subsurface temperature and salinity) using the data assimilation technique described in [Hackert *et al.*, 2014].

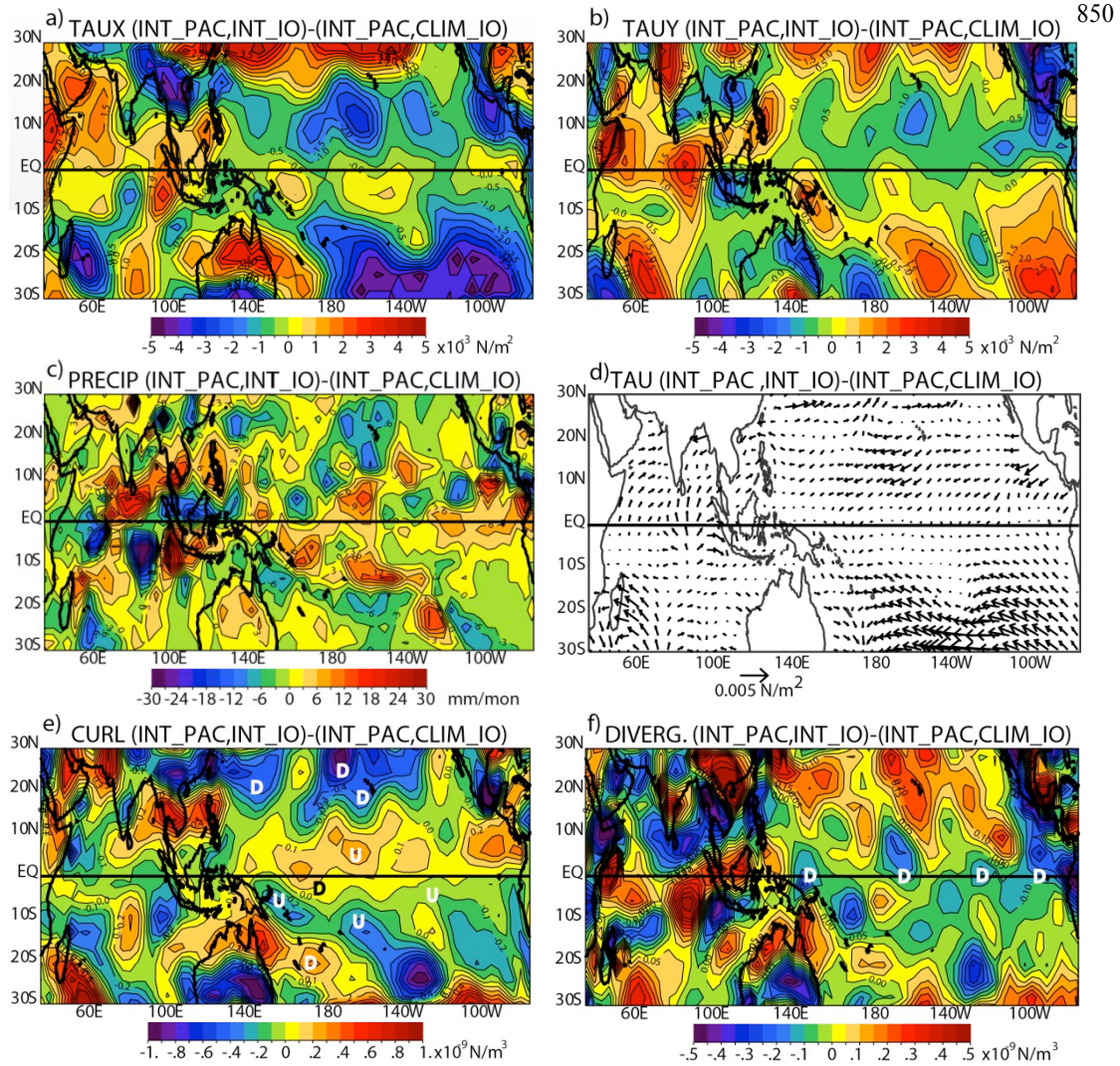


**Figure 2:** Impact of interannual IO SST forcing. Differences between two sets of SPEEDY atmospheric-only experiments for a) zonal, b) meridional wind stress, c) precipitation, d) vector representation of a) and b), e) curl and f) divergence of the wind stress. Differences are full SST anomaly forcing over the Indo-Pacific region (i.e. INT\_PAC, INT\_IO) minus the experiment that uses climatological seasonal cycle forcing over the IO (INT\_PAC, CLIM\_IO). Letters “U” and “D” represent regions of upwelling and downwelling favorable winds and absolute values greater than  $3.3 \times 10^{-3}$  N/m<sup>2</sup>,  $2.7 \times 10^{-3}$  N/m<sup>2</sup>, 13.2 mm/mon,  $0.53 \times 10^{-9}$  N/m<sup>3</sup>,  $0.35 \times 10^{-9}$  N/m<sup>3</sup> are significant at the 95% level for a), b) c), and f), respectively.

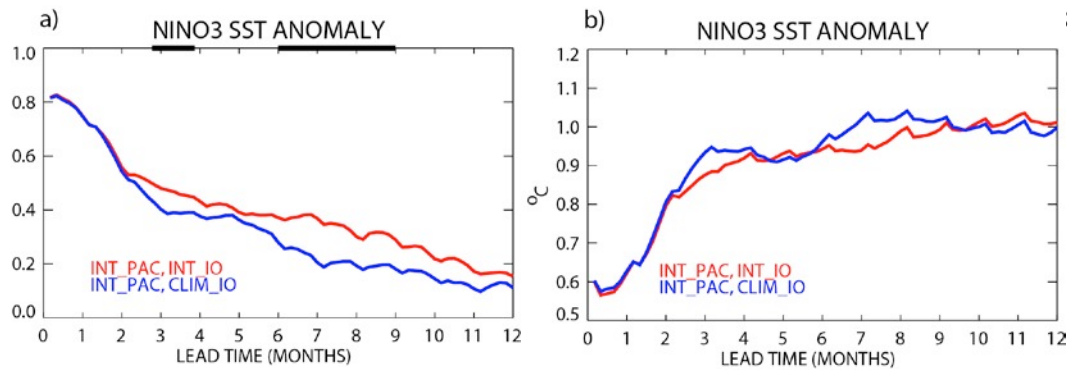


**Figure 3:** Impact of IO interannual forcing on coupled NINO3 SST results.

Validation statistics for a) correlation and b) RMS differences between coupled experiments with full atmospheric coupling (i.e. INT\_PAC, INT\_IO in red and interannual coupling in the Pacific and climatological forcing in the IO (i.e. INT\_PAC, CLIM\_IO) in blue. The coupled experiments are validated against observed NINO3 SST anomaly for 1993 to 2014. Individual correlations exceed the 95% significance out to 8 (43) and 5.8 months (41) (effective degrees of freedom) for red and blue lines, respectively. The thick black line on the top x-axis shows where the red line is significantly larger than the blue line using the Steiger-Z test.

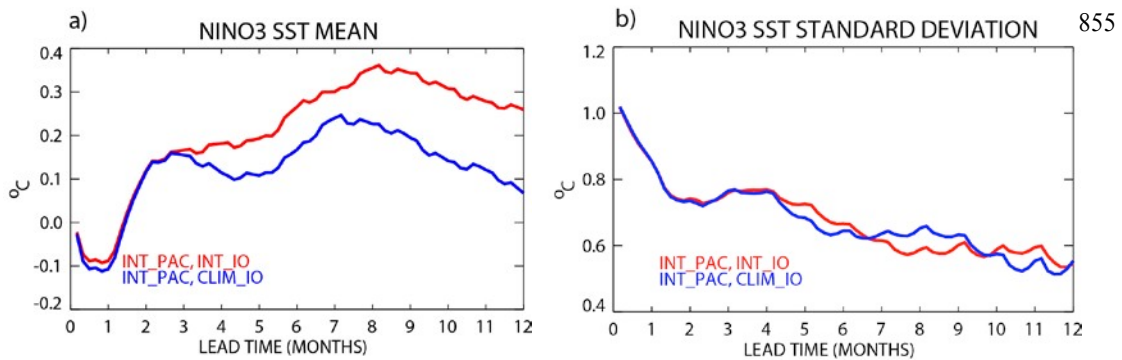


**Figure 4:** Mean and variability of NINO3 SST for impact of interannual IO SST forcing. Plots showing the NINO3 SST a) mean forecast and b) variability for INT\_PAC, INT\_IO (red) and INT\_PAC, CLIM\_IO (blue) for all forecasts from 1993-2014.

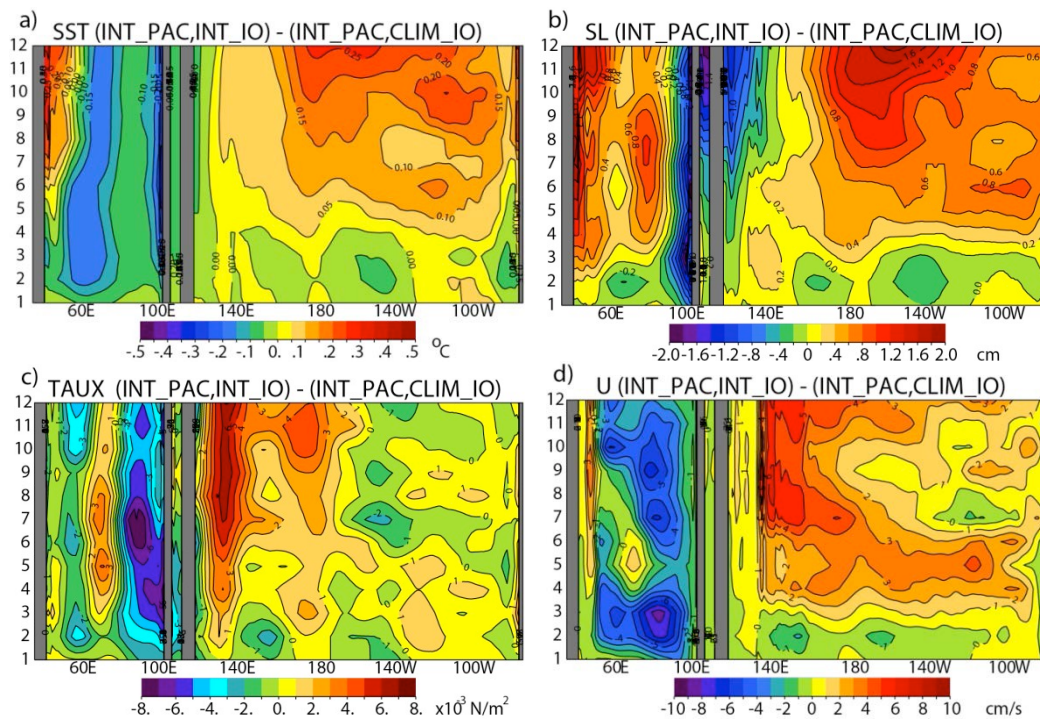


**Figure 5:** Hovmöller plots of impact of interannual IO SST forcing. Plots showing the mean temporal evolution of the impact of IO atmospheric coupling using longitude versus lead time (in months) averaged between  $2^{\circ}\text{N}$  and  $2^{\circ}\text{S}$  for a) SST, b) sea level (SL), c) zonal wind stress, and d) zonal currents. The mean is taken for the average forecast differences, INT\_PAC, INT\_IO minus INT\_PAC, CLIM\_IO, over all months from 1993 to 2014.

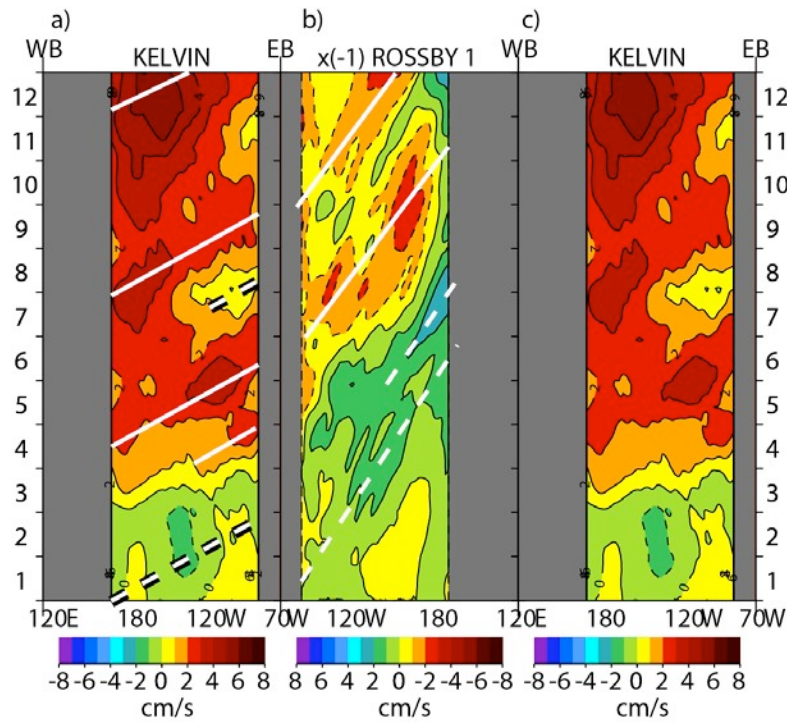


**Figure 6:** Kelvin/Rossby wave decomposition of interannual IO SST forcing. Longitude versus time distribution of the equatorial (a) Kelvin and (b) the first meridional mode of equatorial Rossby waves through their signature in zonal surface current deduced from the average forecast SL differences, (INT\_PAC, INT\_IO) – (INT\_PAC, CLIM\_IO). In order to follow possible wave reflections on the western (WB) and eastern (EB) boundaries, the Rossby panel (b) is inverted and the Kelvin wave pattern is repeated (c). The color scale for the Rossby panel is also inverted since reflection on meridional boundaries results in zonal currents of opposite sign. Solid lines (downwelling) and dashed lines (upwelling) represent theoretical wave speeds for Kelvin (2.5m/s) and Rossby waves (-0.8m/s or ~5months to cross this Pacific basin at 5°N) on each plot.

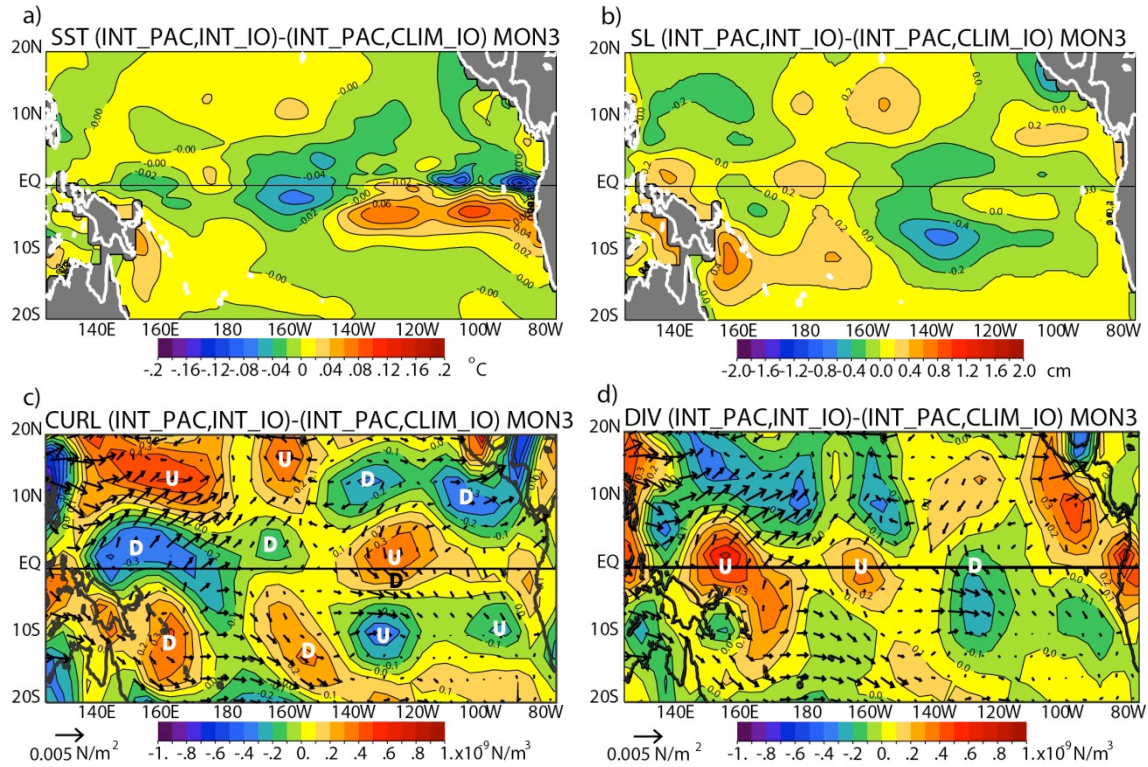


**Figure 7:** Average 3 month forecast INT\_PAC, INT\_IO - INT\_PAC, CLIM\_IO.  
 Average forecast values for month 3 for a) SST, b) sea level, c) curl of the wind stress (color) and wind stress (vector), and d) divergence of the wind stress (color) and wind stress (vector). The scale of the vector plot is indicated in the bottom left of the panel. For the reader's convenience, regions of upwelling and downwelling are marked by letters U and D, respectively.

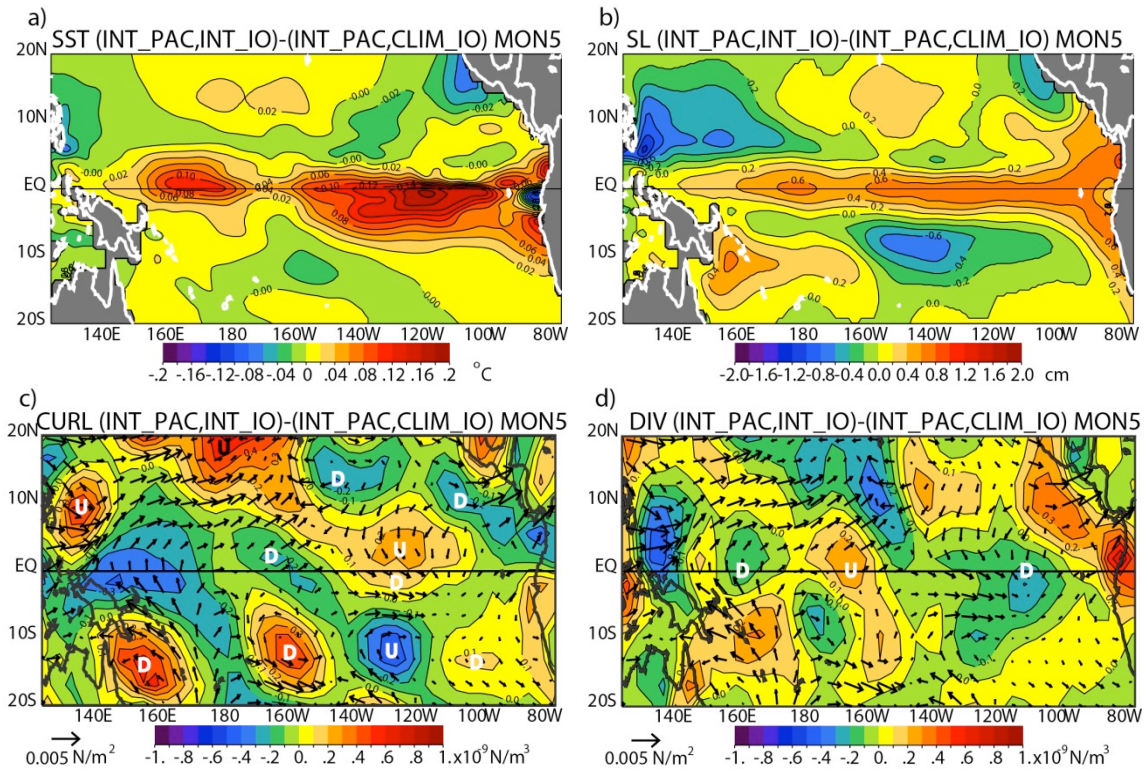
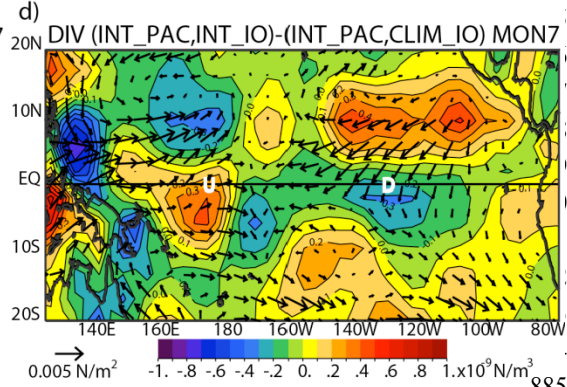
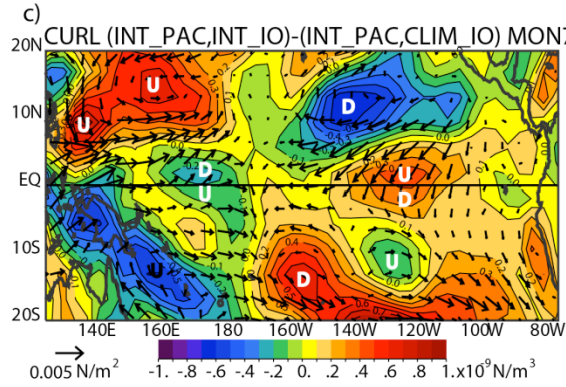
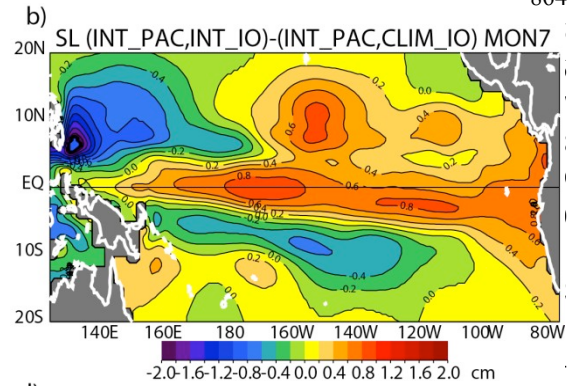
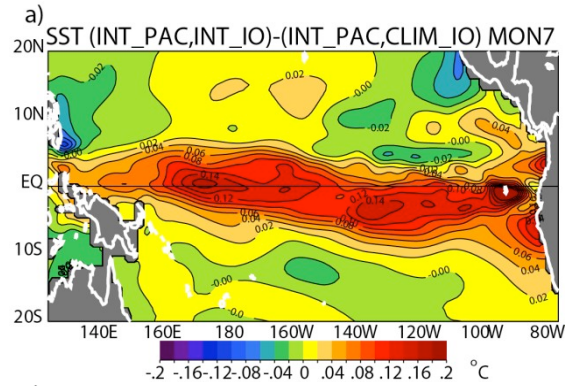


**Figure 8:** Average 5 month forecast INT\_PAC, INT\_IO - INT\_PAC, CLIM\_IO. Same as previous but for 5 month average forecasts.

864



885

**Figure 9:** Average 7 month forecast INT\_PAC, INT\_IO - INT\_PAC, CLIM\_IO. Same as previous but for 7 month lead forecast mean.

886

887

888

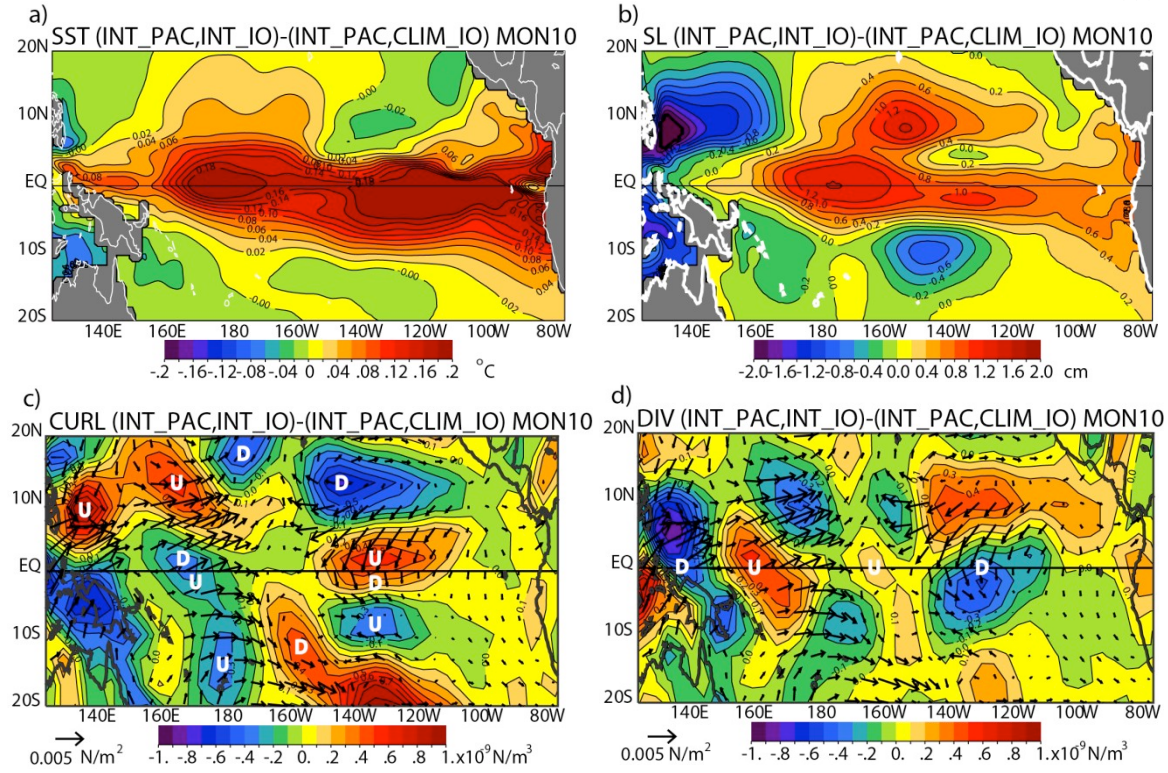


**Figure 10:** Average 10 month forecast INT\_PAC, INT\_IO - INT\_PAC, CLIM\_IO.  
Same as previous but for 10 month forecast mean.